Remote Sensing of Environment 115 (2011) 2931–2942

Contents lists available at ScienceDirect

Remote Sensing of Environment

journal homepage: www.elsevier.com/locate/rse

Estimation of tropical rain forest aboveground biomass with small-footprint lidar and hyperspectral sensors

Matthew L. Clark [a,*], Dar A. Roberts [b], John J. Ewel [c], David B. Clark [d]

[a] Center for Interdisciplinary Geospatial Analysis, Department of Geography and Global Studies, Sonoma State University, Rohnert Park, CA 94928, USA
[b] Department of Geography, University of California, Santa Barbara, Santa Barbara, CA 93106, USA
[c] Department of Biology, University of Florida, Gainesville, FL 32611, USA
[d] University of Missouri-St. Louis, St. Louis, MO, USA

ARTICLE INFO

Article history:
Received 13 July 2009
Received in revised form 29 August 2010
Accepted 31 August 2010
Available online 4 May 2011

Keywords:
Tropical rain forest
Hyperspectral
Small-footprint lidar
Aboveground biomass estimation

ABSTRACT

Tropical forests are an important component of the global carbon balance, yet there is considerable uncertainty in estimates of their carbon stocks and fluxes, which are typically estimated through analysis of aboveground biomass in field plots. Remote sensing technology is critical for assessing fine-scale spatial variability of tropical forest biomass over broad spatial extents. The goal of our study was to evaluate relatively new technology, small-footprint, discrete-return lidar and hyperspectral sensors, for the estimation of aboveground biomass in a Costa Rican tropical rain forest landscape. We derived a suite of predictive metrics for field plots: lidar metrics were calculated from plot vertical height profiles and hyperspectral metrics included fraction of spectral mixing endmembers and narrowband indices that respond to photosynthetic vegetation, structure, senescence, health and water and lignin content. We used single- and two-variable linear regression analyses to relate lidar and hyperspectral metrics to aboveground biomass of plantation, managed parkland and old-growth forest plots. The best model using all 83 biomass plots included two lidar metrics, plot-level mean height and maximum height, with an r^2 of 0.90 and root-mean-square error (RMSE) of 38.3 Mg/ha. When the analysis was constrained to plantation plots, which had the most accurate field data, the r^2 of the model increased to 0.96, with RMSE of 10.8 Mg/ha ($n = 32$). Hyperspectral metrics provided lower accuracy in estimating biomass than lidar metrics, and models with a single lidar and hyperspectral metric were no better than the best model using two lidar metrics. These results should be viewed as an initial assessment of using these combined sensors to estimate tropical forest biomass; hyperspectral data were reduced to nine indices and three spectral mixture fractions, lidar data were limited to first-return canopy height, sensors were flown only once at different seasons, and we explored only linear regression for modeling. However, this study does support conclusions from studies at this and other climate zones that lidar is a premier instrument for mapping biomass (i.e., carbon stocks) across broad spatial scales.

1. Introduction

Tropical forests store a large proportion of terrestrial carbon. For example, Dixon et al. (1994) estimated that low-latitude tropical forests contain 59% and 27% of carbon stored in global forest vegetation and soil pools, respectively. There still remains considerable uncertainty in global and regional estimates of carbon stocks and dynamics. Regional differences in average biomass were up to 40 Mg C/Ha when comparing results from land-use change models to estimates by the FAO for 1980, 1990 and 2000 (Houghton, 2005). This uncertainty in biomass distribution contributes substantial error in estimates of carbon emissions from deforestation, the dominant land-cover change (Houghton, 2005), and forest degradation (Nepstad et al., 1999). Accurate estimates of biomass, particularly at the scale of land-use change, are critical for monitoring carbon dynamics in tropical regions and improving our understanding of the global carbon cycle.

Current methods for biomass estimation include interpolation from relatively small field plots, regional-scale modeling, and remote sensing. These techniques provide estimates of average carbon stocks over a region, but only remote sensing can map the fine-scale variability of biomass over broad spatial extents. Since many important human and natural forest disturbances occur at fine spatial scales, such as selective logging and tree falls, remote sensing has immense potential to improve our understanding of the magnitude of biomass change at multiple scales (Houghton, 2005). Furthermore, remote sensing technology will likely play an important role in monitoring broad-scale carbon stocks and flux within the framework of international policies to reduce greenhouse gases, such as those by the United Nations Framework Convention on Climate Change (UNFCCC) and the newly-funded program for reducing

* Corresponding author.
E-mail address: mateolclark@gmail.com (M.L. Clark).

0034-4257/$ – see front matter © 2011 Elsevier Inc. All rights reserved.
doi:10.1016/j.rse.2010.08.029

emissions from deforestation and forest degradation, or REDD (Angelsen et al., 2009; DeFries et al., 2007; Rosenqvist et al., 2003).

Remote sensing of estimated aboveground biomass (hereafter referred to as biomass) in the tropics has traditionally focused on the use of imagery from passive optical and synthetic aperture radar (SAR) sensors. Broadband indices from passive optical satellite imagery, such as the Normalized Difference Vegetation Index (NDVI), have been correlated with biomass in tropical landscapes (Foody et al., 2003; Sader et al., 1989; Steininger, 2000). However, the relationship typically holds only across young secondary tropical forest types as NDVI saturates with the increased leaf area found in older, structurally complex forests. SAR backscatter responds to the structural and dielectric (i.e., water content) properties of vegetation and, in contrast to optical sensors, penetrates clouds — an important capability in tropical regions. Metrics from SAR are sensitive to biomass for secondary tropical forests up to >60 Mg/ha (Luckman et al., 1997), yet this sensitivity decreases when estimating biomass of denser forests (Imhoff, 1995; Kasischke et al., 1997; Santos et al., 2003). Furthermore, radar applications are limited by terrain, speckle, and surface moisture (Rosenqvist et al., 2003). Recently, Saatchi et al. (2007) demonstrated considerable potential from sensor fusion, in which a binary decision tree was used to select from a combination of SAR and optical variables to estimate biomass over the Brazilian Amazon with an overall accuracy of 81% over a biomass range between 100 and 400 Mg/Ha.

Light detection and ranging (lidar) is a highly successful technology for estimating forest height, volume and biomass (Clark et al., 2004; Drake et al., 2002; Lefsky et al., 2002a, b; Næsset, 1997; Nilsson, 1996). Full-waveform lidar sensors record a detailed height distribution of surfaces illuminated by the laser pulse in footprints from 1 to 80 m and can be found on spaceborne systems, such as the Geoscience Laser Altimeter System (GLAS) sensor on the ICESat satellite (Lefsky et al., 2002b; Lefsky et al., 2007). In contrast, small-footprint lidar sensors record discrete heights at peak returns of light within 0.25- to 0.60-m footprints and are typically flown in helicopters or airplanes (Lefsky et al., 2002b). Small-footprint datasets tend to have high point density and their multiple discrete heights can be used to synthesize a height profile, similar to a waveform, over an area such as a plot or an individual tree (Blair & Hofton, 1999; Lefsky et al., 2002b).

There has been a considerable amount of research using lidar sensors to assess structural properties of temperate and boreal forests, yet few studies come from tropical forests. Drake et al. (2002) used metrics from large-footprint lidar waveforms (LVIS sensor, 25-m diameter footprints) to estimate plot-scale quadratic mean stem diameter, basal area, and biomass over a range of tropical forests at the La Selva Biological Station, Costa Rica. An important metric was the height of median energy (HOME) of the waveform above the mean noise level, which responds to returns from ground and canopy surfaces, and is sensitive to vertical canopy structure and openness. A regression model using HOME to estimate biomass had an r^2 of 0.89, root-mean-square error (RMSE) of 22.5 Mg/ha, and did not saturate with increasing forest height and complexity. In a later study, the HOME metric was not as strong in predicting biomass of seasonally drier tropical forests in Panama (Drake et al., 2003). This lack of generality across sites was attributed to differences in allometric equations used to estimate plot-level biomass from stem diameter at the two sites. Clark et al. (2004) demonstrated the effectiveness of a small-footprint lidar (FLI-MAP sensor used in this study) to estimate mean tree height for plantation plots at La Selva. Plantations with average height from 0.4 to 18.5 m were estimated using plot mean lidar height with a model r^2 of 0.97 and 1.08-m RMSE. Lefsky et al. (2007) presented a new method to estimate forest height from GLAS large-footprint (52 to 90 m) waveforms. The effect of terrain on waveforms was reduced using correction factors derived from field and airborne lidar, and the final cross-site model estimated heights with an r^2 of 0.83 and RMSE of 5 m.

Hyperspectral sensors, or imaging spectrometers, typically measure the electromagnetic spectrum in >100 narrow bands spanning 400 to 2500 nm. Data from these passive sensors are sensitive to forest biochemistry and biophysical properties (Asner, 1998). For tropical and sub-tropical forests, airborne and satellite hyperspectral sensors have been found useful for spectral discrimination of tree species, functional groups and biodiversity (Asner et al., 2008a, b; Carlson et al., 2007; Clark et al., 2005; Kalacska et al., 2007a; Lucas et al., 2008), assessing canopy biochemistry and physiology (Asner et al., 2006; Asner & Vitousek, 2005), and leaf- to canopy-scale structure (Asner et al., 2008a; Kalacska et al., 2007b). It is anticipated that a synergy of information from hyperspectral and lidar sensors can improve estimates of biomass and other forest structure properties, especially if hyperspectral data are used to provide canopy species, phenology, stress and biochemical information (Asner et al., 2007; Asner et al., 2008b; Koetz et al., 2007; Rosenqvist, et al., 2003; Swatantran et al., in press). In a northern temperate forest, Anderson et al. (2008) used LVIS waveform metrics (i.e., HOME) and hyperspectral minimum noise fraction transform (MNF) bands to estimate biomass. The LVIS HOME metric predicted biomass with an r^2 of 0.27, 13 MNF bands predicted biomass with an r^2 of 0.30, while the model r^2 increased to 0.39 with combined lidar and hyperspectral data. Swatantran et al. (in press) examined LVIS waveform metrics and hyperspectral indices and spectral mixture fractions for estimating biomass of Sierra Nevada, California mixed-conifer forests. Biomass was best estimated with lidar metrics over hyperspectral metrics, although there was non-significant evidence that species-level stratification, obtained from hyperspectral analysis, could improve biomass estimates.

The goal of our study was to assess small-footprint lidar and hyperspectral datasets for the estimation of aboveground biomass in a tropical rain forest landscape. We derive a suite of lidar and hyperspectral metrics that were thought to respond to vegetation biomass in tropical and other ecosystems and we use linear regression to estimate plot-scale aboveground biomass from these metrics.

2. Methods

2.1. Study site and materials

2.1.1. Study site

This study was conducted at La Selva Biological Station, a research reserve managed by the Organization for Tropical Studies (OTS) in the Sarapiquí cantón of Costa Rica (84°00′13.0″ W, 10°25′52.5″ N). This site receives on average 4244 mm of precipitation annually, with a relatively dry season from January to April and a second, less severe dry season from August to October, with monthly average precipitation of 217 and 395 mm for the two dry seasons, respectively (Frankie et al., 1974; OTS meteorological data 1957–2006, http://www.ots.ac.cr). The old-growth forest in the reserve is classified as Tropical Wet Forest in the Holdridge Life Zone system (Holdridge, 1971) and includes at least 400 tree species (OTS flora data, http://www.ots.ac.cr).

2.1.2. Field data

We focused our analyses on plots established in old-growth forest and experimental plantations within the reserve (Fig. 1). Old-growth plot data came from 18 0.5-ha long-term study plots, which are randomly placed within three edaphic types: relatively fertile inceptisols on flat, old alluvial terraces, relatively infertile ultisols areas along ridges, and ultisols on steep slopes (CARBONO Project; Clark & Clark, 2000). The plots were mapped within the La Selva grid system and converted to the UTM Zone 16 projection, WGS84 datum using a linear transformation equation (Clark et al., 2004). Each 0.5-ha CARBONO plot (Fig. 1; Fig. 2 — white line in old-growth inset) has x,y locations of tree stems measured relative to each plot's origin. These stems were mapped in the La Selva grid system for each plot, and then all stems were reprojected to the UTM projection. Each 0.5-ha plot (macroplot) was divided into 3 square subplots with 30 m sides (0.09 ha) and spaced 5 m apart (Fig. 2 — solid lines in old-growth). Aboveground biomass for each tree >10-cm diameter within

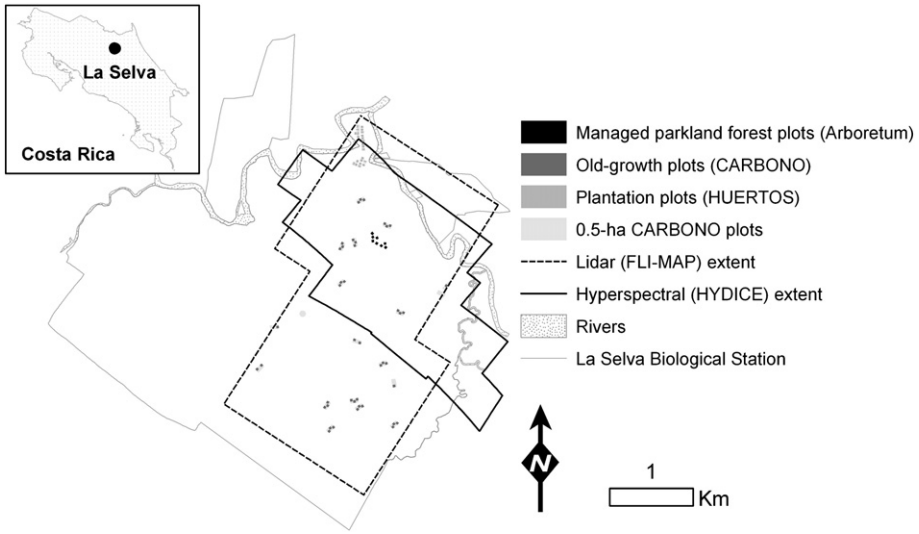

Fig. 1. La Selva Biological Station study site and extent of HYDICE hyperspectral and FLI-MAP lidar datasets.

the subplots was estimated using the tropical wet forest allometric equation (Eq. 1) provided by Brown (1997):

$$\text{biomass} = 21.297 - 6.953(D) + 0.740\left(D^2\right) \quad (1)$$

where D is the tree stem diameter (at 1.3 m or above basal irregularities such as buttresses) and biomass is the estimated oven-dried above-ground biomass (in kg) for the tree. Stem diameter data from a September to early November, 1997 census by the CARBONO crew were used in the biomass calculations ($n = 1950$, $D = 10$–999 cm, mean 447 cm). Note that Eq. (1) is based on 169 trees with diameters from 4 to 112 cm (half from Costa Rica) and does not take into consideration species differences in wood density or structure; and thus, these field data should be considered as estimates and not "ground truth". Plot-level biomass was calculated by dividing the sum of all tree biomass by the subplot area (reported in Mg/ha). Plot biomass values and lidar data come from roughly the same time frame; however, the hyperspectral flight occurred in early 1998, about 5 months after the CARBONO census, and so plot biomass values are lower than would be expected for analyses that use hyperspectral data.

An additional 8 plots of the same dimensions (0.09 ha) were established using stem data acquired in the La Selva's arboretum, a site embedded within old-growth forest on an old alluvial terrace. The arboretum forest has native forest tree species but was cleared of understory vegetation, creating a closed-canopy forest with an herbaceous parkland understory. Stem diameter and x,y data came from a 1993 census, although the data were updated for tree mortality in 1997 (Personal communication, Vargas, 2005). Stem diameters >10-cm were used in calculating biomass (Eq. 1). Arboretum, or "managed parkland forest" plots had haphazard orientations (Fig. 2). The x,y spatial locations of tree stems within these plots were measured in the field with reference to the La Selva grid system and were converted to the UTM projection. These plots are expected to have low estimated biomass values as stem diameter data are from 1993, while our remote sensing data are from 1997 (lidar) and 1998 (hyperspectral).

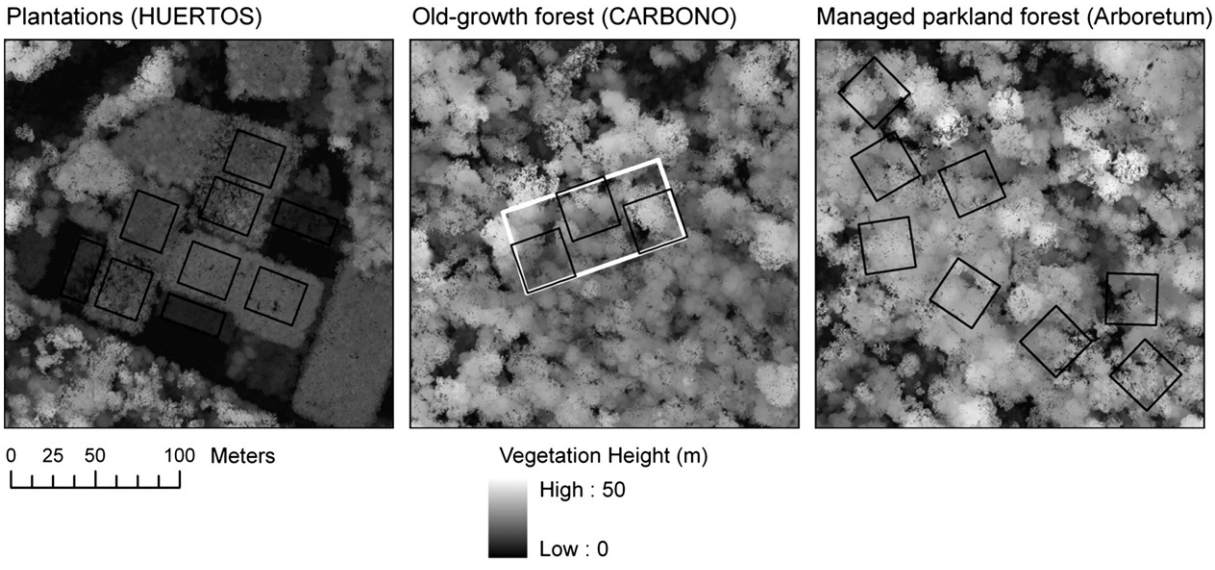

Fig. 2. Example of lidar-derived digital canopy model (DCM) and biomass plots for plantations, managed parkland forest and old-growth forest. The white line in old-growth forest represents 0.5-ha CARBONO macroplot plot containing three 30×30-m subplots, black lines (see Methods).

Plantation plot data were acquired by the HUERTOS Project in a May–June, 1997 census (Menalled et al., 1998; plus unpublished data). The plots were monocultures on 1-year (n = 9; 0.04 ha each) or 4-year (n = 9; 0.08 ha each) cutting cycle, or monocultures and polycultures that were uncut (n = 14; 0.12 ha each) (Fig. 2 — plantations). Trees were 2 m apart in all plots. At the time of the census, nine plots contained 1-yr-old vegetation, nine had 2-yr-old vegetation, and 14 had 6-yr-old vegetation. The dominant tree species were *Hyeronima alchorneoides* (Euphorbiaceae), *Cedrela odorata* (Meliaceae), or *Cordia alliodora* (Borginaceae). Seven of the 14 uncut plots included a mixture of one of the three tree species as well as a sub-canopy palm, *Euterpe oleracea* (mean height 7.13 m), and a smaller understory herb, *Heliconia imbricata* (mean height 1.53 m). The total aboveground biomass for each individual plant was the sum of biomass estimated for tissue components: leaves, rachises (for *Cedrela* and *Euterpe*), branches, and boles (main stems). These component parts were estimated with species allometric equations based on stem diameter, height, and number of shoots (for *Euterpe* and *Heliconia*) that were developed using destructive-harvest data from the site (Cole & Ewel, 2006). Equations for biomass components of *Cedrela*, *Cordia*, *Eutrepe* and *Hyeronima* are published in Cole and Ewel (2006), while *Heliconia* equations used were:

$$Leaf\ (leaf\ blades):\ biomass = 0.148(H \times S)^{1.188} \quad (2)$$

$$Stem\ (petioles\ \&\ stems):\ biomass = 0.105(H \times S)^{1.325} \quad (3)$$

$$Inflorescence\ (flowers,\ large\ bracts,\ \&\ fruits):\ biomass = 1.008(H \times S)^{0.681} \quad (4)$$

where biomass is estimated dry weight in grams per clump (many genets per clump), H is the clump height in cm and S is the integer count of shoots in a clump. Plot-level biomass was calculated by summing all plant biomass in the plot and dividing by ground-measured area (Mg/ha). The two-dimensional area of each plantation plot was generated in a GIS with field specifications and then each plot was visually georeferenced to the lidar DCM and hyperspectral datasets as separate layers. No visual georeferencing was performed for old-growth or managed parkland plots.

2.1.3. Lidar data

Lidar data were from the FLI-MAP sensor (John E. Chance & Associates, Lafayette, Louisiana), which measured the first single-return height above noise level in small footprints (~30 cm) with a 0.9-μm laser and a typical density of 9 points/m^2 (see Clark et al., 2004 for more details). The data were acquired from a helicopter in September 12 and 13, 1997 (Fig. 1), during the shorter, less pronounced dry season. Note that the flight date was incorrectly identified as October, 1997 in Clark et al., 2004. The original FLI-MAP lidar surface was processed to a raster surface, or digital canopy model (DCM), measuring maximum vegetation height in 0.33-m cells (Clark et al., 2004). These data were analyzed in the UTM projection, Zone 16 North with WGS84 datum.

2.1.4. Hyperspectral data

This study used 1.6-m spatial resolution, hyperspectral reflectance imagery from the HYDICE (Hyperspectral Digital Imagery Collection Experiment) airborne sensor (image extent shown in Fig. 1). The HYDICE sensor measures 210 bands covering the 400–2500 nm region of the electromagnetic spectrum (Basedow et al., 1995). HYDICE data were acquired on March 30, 1998, at the end of the more pronounced dry season. Atmospheric correction and orthorectification processing of the imagery to the UTM Zone 16 North projection is described in Clark et al. (2005). After removing bands with significant noise (e.g., atmospheric water absorption windows), the final dataset had 161 bands.

2.2. Lidar metrics

The DCM cell values within plots (0.04 to 0.13 Ha) were used to calculate a suite of lidar metrics from the resulting plot vertical height profile, or height histogram. These metrics included the mean height (MeanHgt), mean of the 95th percentile of heights (Mean95pct), median height (MedHgt), maximum height (MaxHgt), standard deviation of heights (StdDevHgt), kurtosis, skewness, and the median to maximum height ratio (MedMax). In addition, the percent of the plot occupied by gaps (PctGap) was estimated by classifying gap cells as those having a height less than 5 m height.

2.3. Hyperspectral metrics

Plot-level hyperspectral data were calculated by averaging spectra from pixels within each plot. From these plot spectra, we computed a suite of hyperspectral metrics–narrowband indices and spectral mixture fractions–that respond to photosynthetic pigment, water and other biochemical absorption features across the visible (VIS = 437–700 nm), near infrared (NIR = 700–1327 nm) and shortwave infrared (SWIR = 1467–2435 nm) regions of the electromagnetic spectrum. Plot-level hyperspectral metrics were then used in regression analyses (Section 2.4).

2.3.1. Photosynthetic vegetation, structure, senescence and health indices

Metrics sensitive to photosynthesis and vegetation structure included narrowband versions (Table 1) of the Simple Ratio Vegetation Index (SR; Jordan, 1969; Tucker, 1979), Normalized Difference Vegetation Index (NDVI; Rouse et al., 1973; Tucker, 1979), Soil Adjusted Vegetation Index (SAVI: Huete, 1988), and Enhanced Vegetation Index (EVI; Huete et al., 2002). SR and NDVI theoretically respond to canopy chlorophyll concentration and absorption of red light, and scattering of NIR photons within vegetation structure, making these indices empirically correlated with leaf area index (LAI) and absorbed photosynthetically active radiation (FPAR), respectively (Elvidge & Chen, 1995; Hall et al., 1992; Myneni et al., 1995; Spanner et al., 1994). NDVI tends to saturate in high biomass areas or in periods of maximum LAI, and is sensitive to the brightness of background reflectance (Huete et al., 1985; Spanner et al., 1994; Wang et al., 2005). SAVI (Huete, 1988) is a modified form of the NDVI shown to be less sensitive to variation in background reflectance. EVI has greater sensitivity than NDVI in areas

Table 1
Formulas for narrowband indices (ρ is reflectance at a specific wavelength in nm). Wavelengths chosen are the closest HYDICE wavelengths to the formulas in the cited literature.

Photosynthetic vegetation, structure, senescence and health	
Simple Ratio	Tucker, 1979
SR = ρ798 / ρ679	Jordan, 1969
Normalized Difference Vegetation Index	Tucker, 1979
NDVI = (ρ798 − ρ679) / (ρ798 + ρ679)	Rouse et al., 1973
Enhanced Vegetation Index	Huete et al., 2002
EVI = (ρ798 − ρ679) / (1 + ρ798 + 6 ρ679 − 7.5 ρ482)	
Soil-Adjusted Vegetation Index	Huete, 1988
SAVI = (1.5 ρ798 − ρ679) / (ρ798 + ρ679 + 0.5)	
Red-Edge Vegetation Stress Index	Merton & Huntington., 1999
RVSI = [(ρ719 + ρ752) / 2] − ρ730	
Plant Senescence Reflectance Index	Merzlyak et al., 1999
PSRI = (ρ679 − ρ501) / ρ752	
Water and lignin content	
Water Band Index	Peñuelas et al., 1997
WBI = ρ902 / ρ973	
Normalized Difference Water Index	Gao, 1996
NDWI = (ρ862 − ρ1239) / (ρ862 + ρ1239)	
Normalized Difference Lignin Index	Serrano et al., 2002
NDLI = [log(1/ρ1748) − log(1/ρ1675)] / [log(1/ρ1748) + log(1/ρ1675)]	

with high leaf area (i.e., does not saturate) and is designed to reduce the influence of background reflectance and atmospheric noise in the vegetation signal (Huete et al., 2002).

We included two indices that respond to vegetation phenology and health: (Table 1) Red-edge Vegetation Stress Index (RVSI: Merton & Huntington., 1999) and Plant Senescence Reflectance Index (PSRI; Merzlyak et al., 1999). RVSI quantifies changes in the position of the red-edge in response to plant stress and seasonal changes in chlorophyll content (Merton & Huntington., 1999). RVSI is also positively correlated with leaf biomass (Perry & Roberts, 2008). PSRI is sensitive to the ratio of carotenoids and chlorophyll in leaves and tracks senescence-induced degradation of chlorophyll (Merzlyak et al., 1999).

2.3.2. Canopy water and lignin indices

Green (live) vegetation reflectance in the 900 to 2500 nm region of the spectrum is heavily influenced by water absorption bands. Absorption features in the NIR, at 970 nm and 1240 nm, are particularly useful for quantifying vegetation water content because absorption does not saturate with increasing water concentration. Hyperspectral research has shown that metrics based on NIR water-absorption bands correlate with vegetation moisture content and structure of canopy components (Dennison et al., 2003; Roberts et al., 2004; Serrano et al., 2000). We explored two NIR water-absorption indices for biomass estimation (Table 1): Water Band Index (WBI; Peñuelas et al., 1997) and the Normalized Difference Water Index (NDWI; Gao, 1996), which measure the 970-nm and 1240-nm water-absorption features, respectively. These indices are not influenced by chlorophyll absorption, so they are complementary to vegetation indices based on red absorption, i.e., SR, NDVI, EVI (Gao, 1996).

Several other vegetation biochemicals, such as lignin and cellulose, create absorption features across the SWIR region measured by hyperspectral sensors (Curran, 1989; Elvidge, 1990). In this study we explored the Normalized Difference Lignin Index (NDLI; Serrano et al., 2002; Table 1). When tested with hyperspectral imagery from chaparral communities in southern California, Serrano et al. (2002) found that NDLI was sensitive to both bulk canopy lignin and vegetation structure of green continuous canopies, although the relationship was not significant for senescing canopies or ecosystems with exposed soil (low leaf area).

2.3.3. Spectral mixture analysis

We estimated fractional abundance of green vegetation (GV), non-photosynthetic vegetation (NPV) and shade spectral endmembers for plot-scale spectra using spectral mixture analysis (SMA; Roberts et al., 1993; reviewed in Keshava & Mustard, 2002). As opposed to narrowband indices, SMA endmember fractions are modeled using full-spectrum information (i.e., 161 bands, 437 to 2435 nm). Few studies in tropical ecosystems have linked endmember fractions to forest biophysical parameters, such as biomass. However, Hall et al. (1995) showed that SMA shade and background fractions were strongly related to biomass, LAI, DBH and net primary productivity in boreal conifer-dominated forests, while sunlit canopy fraction (e.g., GV) and NDVI were not as predictive. In a comprehensive comparison of SMA endmembers and 10 vegetation indices calculated from Landsat-simulated imagery, the shadow fraction consistently outperformed broad-band indices in estimating boreal forest biomass, leaf-area index (LAI), NPP, DBH, stem density, and basal fraction (Peddle et al., 2001). Studies from non-forest sites have employed hyperspectral data in their analyses of vegetation biophysical parameters (Asner & Lobell, 2000; McGwire et al., 2000; Sonnentag et al., 2007). In estimating percent green cover in an arid environment, McGwire et al. (2000) showed that the GV endmember fraction modeled 10% more variance than the best of several broad-band and narrow-band vegetation indices.

Details of our SMA method are described in Clark, 2005 (Chapter 4) and are summarized below. A GV endmember was selected by plotting selected crown pixels in a red vs. NIR scatter plot. Thirteen pixels with relatively low red and high NIR were averaged to form one GV image endmember, and nine pixels with high red and low NIR were averaged to form one NPV image endmember. The NPV image spectrum was a mixture of spectral properties from NPV (e.g., bark) and GV (e.g., tree leaves, canopy epiphytes, and moss) measured within the sensor's instantaneous field of view (IFOV). We used a photometric shade endmember with a uniform reflectance of zero. A library of 102 field and laboratory spectra was included in the analysis to allow the selection of a purer NPV endmember spectrum. An NPV endmember was selected from the library using the criteria that it yield a low model root-mean-square error (RMSE) and provide physically reasonable fractions when combined with the image GV endmember to unmix the image NPV endmember (Roberts et al., 1993). The final NPV reference endmember ultimately selected was from a tree trunk spectrum acquired in the field at La Selva. The GV, NPV and shade endmembers were then applied in a SMA to plot-level hyperspectral data (Section 2.3), producing fractional abundance of each endmember for each plot.

2.4. Statistical analyses

We used regression analyses to relate plot-scale lidar and hyperspectral metrics to field-derived biomass from all plots and plantation plots only. There were 83 plots located within the lidar DCM, while only 39 of these plots were in the hyperspectral imagery; thus there were 39 total samples (15 were plantation) for regression models with hyperspectral metrics or lidar combined with hyperspectral metrics (Table 2).

Ordinary least squares (OLS) regression assumes that error residuals from the model are not autocorrelated. Field plot centroids (i.e., centers) were located an average 1500 m and maximum 3670 m apart, yet the minimum inter-plot distance was 14 m; therefore, some residuals could be spatially autocorrelated at short distances (Cressie, 1993). There are several examples of autocorrelated error in our lidar and hyperspectral datasets, including spatial variation in georeferencing accuracy of imagery and field plots, changing atmospheric conditions and radiometric calibration along flight lines, and differences in ground retrieval accuracy, and subsequent vegetation height estimation, across land-cover types (Clark et al., 2004). To accommodate residual autocorrelation, we used a form of generalized least squares (GLS) regression that weights residuals based on an error variance–covariance matrix. The residual covariance is estimated by passing the spatial distance between sample pairs through a modeled spatial covariance function (e.g., a model variogram). Methods followed those in Lark (2000) and Lark and Cullis (2004) and were automated with the *R* statistical software v2.9.0 (R Development Core Team, 2005 and its *geoR* v1.6-25 (Ribeiro & Diggle, 2001) and *nlme* v3.1-91 packages (Pinheiro & Bates, 2000). Single-predictor GLS regression proceeded as follows: 1) a remote sensing metric (e.g., MeanHgt and NDVI) was regressed against biomass using OLS regression; 2) an empirical variogram was calculated from the OLS residuals, with plot centroids

Table 2
Summary of field-measured aboveground biomass (Mg/ha) for plots located on the lidar image (n = 83) and both lidar and hyperspectral images (n = 39).

	Average	Std Dev	Min	Max	n
Lidar plots					
Managed old-growth	193.3	69.0	98.0	271.6	8
Old-growth	168.5	52.3	76.4	278.9	43
Plantation	30.7	33.1	0.04	93.5	32
All plots	117.8	84.2	0.04	278.9	83
Lidar and hyperspectral plots					
Managed old-growth	193.3	69.0	98.0	271.6	8
Old-growth	162.6	51.7	76.4	230.2	16
Plantation	31.5	32.5	0.04	87.1	15
All plots	118.4	85.5	0.04	271.6	39

serving as *x,y* point coordinates and the maximum variogram lag distance set at 2/3 of the greatest distance between plot centroids; 3) initial model residual variogram parameters were set to: range equal to the maximum lag distance, sill equal to semivariance at the range, and the nugget equal to 1/2 the lowest semivariance; 4) the residual variogram range, sill and nugget parameters were then re-estimated using the *variofit* function in *geoR*; and 5) remote sensing metrics were then GLS regressed against biomass using the *gls* function in the *nlme* package. In the *gls* function, the OLS residual variogram parameters were used only as initial states, as they are biased (Cressie, 1993). These spatial covariance parameters were re-estimated simultaneously with regression-model fixed effects using the Residual Maximum Likelihood (REML) method and simulated annealing optimization (Lark & Cullis, 2004). Steps 4 and 5 were performed separately with a Spherical and Exponential spatial covariance function, and the best function was determined based on the overall GLS regression r^2 value and whether the REML-estimated range was less than the maximum distance between plot centroids. If both Spherical and Exponential range estimates were too large, then only the OLS regression results were reported. The covariance function selected was used in a leave-one-out cross validation of samples to establish a root-mean-square error (RMSE) for the regression model. This cross validation approach was also used to calculate RMSE for the associated OLS regression model.

The GLS procedure described above was also performed for every combination of two predictor metrics (e.g., multiple regression). All GLS regression models were also tested with a square root (SQRT) transform applied to biomass. In this case, the model RMSE was reported in the original biomass units Mg/ha (not square root). The best three GLS models were ranked, in order: 1) valid range parameter, 2) high r^2, and 3) low RMSE. Parameters for the starting OLS model of the selected GLS models were also reported.

2.5. Mapping biomass

To map biomass across the landscape with lidar metrics, we overlaid a 30×30-m grid over the DCM. Each grid cell was thus the same size as a CARBONO subplot and contained 8100 0.33-m DCM vegetation heights. Lidar metrics were calculated from DCM heights in each 30×30-m cell. We then applied to each grid cell the best GLS regression model with lidar metrics and all plots.

3. Results

3.1. Field-measured biomass

Estimates of biomass from field plot data ranged from 0.04 to 278.9 Mg/ha (Table 2). Old-growth forest plots tended to have more biomass than plantations (average). Old-growth forest biomass was more variable than plantations in terms of standard deviation; however, the coefficient of variation (c.v.) is considerably lower in old-growth forest compared to plantations (31% vs. 108%). The high c.v. among plantations undoubtedly reflects the mix of ages (1 to 6 years) and species composition they comprised. Within a forest type, plantations are more variable in percentage terms, but not in absolute biomass terms, since the average biomass of old growth is over five times higher.

Plantation plots were highly dynamic, with trees undergoing rapid growth. The HUERTOS field data used for biomass estimation were measured 72–111 days before the lidar acquisition in September, 1997 (Section 2.1.3), while they were 269–308 days before the hyperspectral data acquisition in March, 1998. When compared to a May–June,1998 census, the annual growth in biomass was on average 9.8 ± 6.4 Mg/ha (maximum = 16.7 Mg/ha). We thus expect that our field-based biomass values from plantation plots (except 1-yr rotation plots) are lower than values from plots measured at the same time as the hyperspectral and lidar flights. Nine plots had annual harvesting and replanting shortly after the May–June 1997 inventory. For these plots, field biomass values were likely too high as we matched peak biomass, measured in the field immediately prior to harvest, to remote sensing data acquired when biomass was recovering after harvest.

3.2. Estimation of biomass — all plots

Estimation of biomass with lidar was performed using all plots available in FLIMAP imagery and with all plots that were also located within the HYDICE and FLIMAP images. The best single-variable GLS regression model from all 83 plots on FLIMAP was using MeanHgt and the square-root of biomass, SqrtBiomass (Table 3, Fig. 3: $r^2 = 0.88$; RMSE = 38.6 Mg/ha). The OLS regression model had a slightly stronger r^2 of 0.89, yet its RMSE was 1.7 Mg/ha higher than the GLS model. This trend of 0.01 lower r^2 with slightly lower RMSE for GLS relative to OLS regression was a consistent pattern for all lidar models (Table 3).

Table 3
One- and two-variable regression models to estimate aboveground biomass from lidar metrics. All model parameters are for ordinary least-squares (o) followed by generalized least-squares (g) regression models. Structure, nugget and range (in meters) are residual-variogram model parameters for generalized least-squares regression.

Rank	Trans[a]	X1	X2	r^2(o)	RMSE(o)[b]	r^2(g)	RMSE[b](g)	Intercept	Slope X1	Slope X2	Str[c]	Nugget	Range
Lidar metrics — all plots located on FLIMAP image (n = 83)													
One predictor variable													
1	Sqrt	MeanHgt	–	0.89	40.3	0.88	38.6	1.14/2.17	0.55/0.51	–	Sph	0.38	510.7
2	Sqrt	Mean95pct	–	0.87	43.5	0.87	43.2	0.86/1.26	0.37/0.36	–	Sph	0.91	1489.2
3	Sqrt	MedianHgt	–	0.87	43.6	0.86	41.0	1.32/2.60	0.52/0.47	–	Exp	0.43	387.1
Two predictor variables													
1	Sqrt	MeanHgt	MaxHgt	0.90	39.3	0.90	38.3	0.72/1.54	0.43/0.44	0.08/0.06	Sph	0.39	748.0
2	Sqrt	MeanHgt	MedianHgt	0.90	39.5	0.89	38.0	1.05/2.00	1.30/0.88	−0.72/−0.35	Exp	0.51	496.4
3	Sqrt	MeanHgt	StdDevHgt	0.90	40.1	0.89	38.7	1.01/1.81	0.49/0.49	0.20/0.10	Exp	0.35	279.8
Lidar metrics — all plots located on both FLIMAP and HYDICE images (n = 39)													
One predictor variable													
1	Sqrt	Mean95pct	–	0.91	36.0	0.91	35.8	0.57/0.23	0.38/0.39	–	Sph	0.35	266.0
2	Sqrt	MeanHgt	–	0.89	39.0	0.88	37.2	1.22/2.17	0.52/0.49	–	Exp	0.39	1050.0
3	Sqrt	MedianHgt	–	0.88	41.2	0.86	39.3	1.40/2.34	0.48/0.46	–	Exp	0.21	152.9
Two predictor variables													
1	Sqrt	Mean95pct	StdDevHgt	0.93	33.7	0.92	33.2	0.54/0.48	0.49/0.50	−0.52/−0.51	Exp	0.36	325.1
2	Sqrt	MeanHgt	Mean95pct	0.92	34.5	0.92	34.3	0.65/0.58	0.21/0.24	0.23/0.22	Sph	0.28	320.8
3	Sqrt	Mean95pct	MedianHgt	0.92	35.6	0.91	35.5	0.64/0.53	0.27/0.25	0.14/0.19	Sph	0.38	384.6

[a] Sqrt = square-root transformation of biomass.
[b] RMSE = root mean-squared error in biomass units, Mg/Ha, including for Sqrt models.
[c] Correlation structure of residuals, Sph = Spherical or Exp = Exponential.

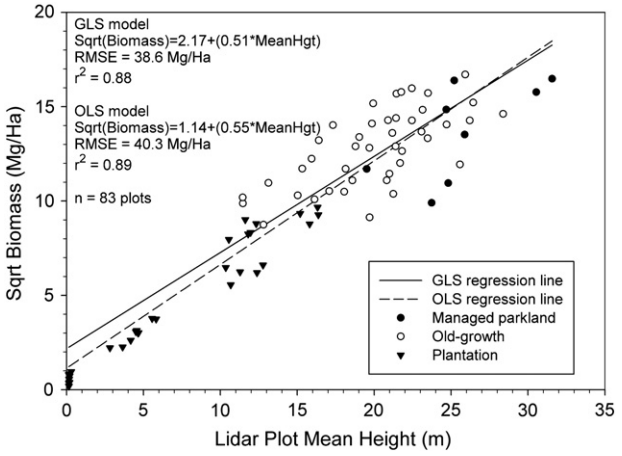

Fig. 3. Best single-variable model for estimating biomass from lidar metrics. Predictor variable is plot mean height (MeanHgt) and the response is the square-root of plot-level biomass. Models are for ordinary (OLS) least-squares and general least-squares (GLS) regression.

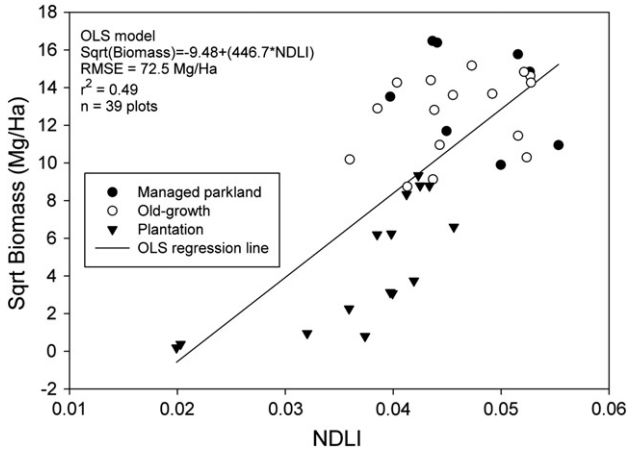

Fig. 4. Relationship between the normalized difference lignin index (NDLI) and plot-level biomass (square-root).

Accounting for autocorrelation in residuals from plot proximity appeared to strengthen models by reducing overall error.

Regression models with two lidar metrics all had MeanHgt and the addition of MaxHgt, MedianHgt or StdDevHgt (Table 3, n = 83). Relative to the single-variable model with MeanHgt, the addition of MaxHgt improved the GLS r^2 from 0.88 to 0.90, yet the RMSE only improved by 0.3 Mg/ha.

When considering the 39 plots on both the lidar and hyperspectral images, the best single-variable GLS model used Mean95pct and had a slightly improved fit ($r^2 = 0.91$ and RMSE = 35.8 Mg/ha) relative to the best 83-plot model (Table 3). Models from 39 plots are presented for comparison with hyperspectral analysis; however, we consider the models from 83 plots more robust since they have twice the sample size.

Single-variable models using hyperspectral metrics had r^2 values that ranged from 0.36 to 0.49 with NDLI and PSRI as predictors (Table 4). Fig. 4 shows the relationship between NDLI and SqrtBiomass, which was the best model with a single hyperspectral metric. The best two-variable models had r^2 values from 0.57 to 0.68 and RMSE from 64.4 to 71.3 Mg/ha, with WBI and EVI as predictors in the best model. As with lidar models, the square-root of biomass tended to improve the linear fit.

Models that used a lidar and hyperspectral metric had no improvement over models with 2 lidar metrics, with r^2 values of 0.91 and RMSE from 35.4 to 36.6 Mg/ha (Table 5). The top three GLS models used the Mean95pct lidar metric in combination with the PSRI, SR or WBI hyperspectral metrics.

3.3. Estimation of biomass — plantation plots only

Table 6 shows the top plantation models, similar to Rank 1 in Tables 3–5, but only considering plantation plots. Note that OLS regression was used because there were fewer plots to fit the necessary GLS regression parameters. As with the analysis with all plots, MeanHgt was the best single variable for estimating plantation biomass, and the model was stronger (Fig. 5: $r^2 = 0.95$; n = 32) than when using all plots (Fig. 3: $r^2 = 0.89$; n = 83). In contrast, the MeanHgt model was weaker when limited to old-growth plots (Fig. 5: $r^2 = 0.43$; n = 51). The overall MeanHgt model, which covers the full range of La Selva forest biomass from plantations to old-growth, was thus heavily dependent upon the lower biomass plantation plots to provide an accurate fit.

There were only 15 plots available for assessing combined lidar and hyperspectral metrics for plantation biomass. For hyperspectral metrics, EVI was the best single predictor, while GV and NDWI were important for a two-variable model (Table 6). The best two-variable model with lidar metrics had a high r^2 of 0.98 and low RMSE of 8.1 Mg/ha (n = 15). The best model with a lidar and hyperspectral metric had the same r^2, with slightly 0.6 Mg/ha RMSE.

4. Discussion

4.1. Comparison of lidar and hyperspectral metrics for estimating biomass

For the lidar and hyperspectral metrics analyzed in this study, those derived from lidar vegetation height (i.e., DCM) were the strongest predictors of biomass. The mean plot height metric (MeanHgt) had the

Table 4
One- and two-variable regression models to estimate aboveground biomass from hyperspectral metrics. Residual correlation structure could not be estimated for general least-squares regression, so all model parameters are for ordinary least-square regression (o).

Rank	Transform[a]	X1	X2	r^2(o)	RMSE(o)[b]	Intercept	Slope X1	Slope X2
Hyperspectral metrics — all plots located on both FLIMAP and HYDICE images (n = 39)								
One predictor variable								
1	Sqrt	NDLI	–	0.49	72.5	−9.48	446.66	–
2	Sqrt	PSRI	–	0.40	77.2	13.16	−70.81	–
3	None	NDLI	–	0.36	70.3	−166.95	6635.99	–
Two predictor variables								
1	Sqrt	WBI	EVI	0.68	64.4	40.27	−38.14	167.20
2	Sqrt	GV	WBI	0.68	66.3	46.46	0.03	−41.02
3	Sqrt	WBI	NDVI	0.57	71.3	7.62	−26.59	38.29

[a] None = no transformation of biomass; Sqrt = square-root transformation of biomass.
[b] RMSE = root mean-squared error in biomass units, Mg/Ha, including for Sqrt models.

Table 5
Two-variable regression models to estimate aboveground biomass from lidar and hyperspectral metrics. All model parameters are for ordinary least-squares (o) followed by generalized least-squares (g) regression models. Structure, nugget and range (in meters) are residual-variogram model parameters for generalized least-squares regression.

Rank	Trans[a]	X1	X2	r^2(o)	RMSE(o)[b]	r^2(g)	RMSE(g)[b]	Intercept	Slope X1	Slope X2	Str[c]	Nugget	Range
Lidar + hyperspectral metrics — all plots located on both FLIMAP and HYDICE images (n = 39)													
1	Sqrt	Mean95pct	PSRI	0.91	35.8	0.91	35.4	1.39/1.02	0.36/0.37	−8.14/−4.98	Sph	0.18	135.6
2	Sqrt	Mean95pct	SR	0.92	36.2	0.91	35.6	−0.34/0.10	0.37/0.37	0.07/0.07	Sph	0.17	1907.9
3	Sqrt	Mean95pct	WBI	0.91	36.9	0.91	36.5	−1.42/−4.47	0.38/0.39	1.58/4.30	Sph	0.28	271.6

[a] Sqrt = square-root transformation of biomass.
[b] RMSE = root mean-squared error in biomass units, Mg/Ha, including for Sqrt models.
[c] Correlation structure of residuals, Sph = Spherical or Exp = Exponential.

best model when regressed against the square-root of biomass (SqrtBiomass). The linear fit between SqrtBiomass and MeanHgt was stronger with plantation plots than with old-growth plots, which can be attributed to several factors. Plantations have an even-aged tree structure, which yields less variation in stem height and density for a given level of plot biomass. Lidar-derived canopy height (DCM) was also more accurately estimated for plantations than old-growth forest (Clark et al., 2004). In contrast, old-growth stands have more variability in stem height and density within plots and less accurate lidar-derived heights (Clark et al., 2004). These factors translate into less variable lidar heights within a plot (Fig. 2 — plantation) and less variation in plot mean lidar height for plantation biomass values (Fig. 4). There were also important differences in when and how field biomass was measured. Individual tree biomass in plantations was calculated from relatively accurate species-level allometric equations, although data were from 3 months prior to the lidar flight. Old-growth and parkland forest plot biomass was estimated from a less accurate, generalized allometric equation (Eq. 1), and the 8 parkland plots had biomass measured 4 years prior to the lidar flight. Thus, relatively low variation in mean plot height for levels of biomass, coupled with more accurate biomass field measurements, is expected to strengthen the linear model for plantation samples and reduce RMSE (Fig. 5 — plantation). Old-growth forest structure is spatially autocorrelated at relatively short distances (Clark et al., 1996), which means that a slight spatial mismatch between field and lidar plot locations could cause relatively large errors in connecting estimates of mean canopy height to biomass values. All of these factors are expected to cause more variable lidar mean height for similar levels of biomass in old-growth forest, and larger model RMSE (Fig. 4 — old-growth forest).

In terms of variance explained, our MeanHgt biomass model (all plots) from small-footprint, discrete-return lidar was similar to the large-footprint, waveform-based (LVIS) model in Drake et al. (2002), also from La Selva ($r^2 = 0.88$, FLIMAP vs. $r^2 = 0.89$, LVIS). However, the RMS error was lower with the LVIS model (22.5 Mg/ha) than with FLIMAP model (38.6 Mg/ha). Drake and colleagues used the average HOME value from footprints found entirely in field plots, while our study used mean of estimated vegetation height from 0.33 m cells covering the whole plot. The Drake et al. model included 34 plots that ranged in size from 0.05 to 0.5 ha, while our model used 83 plots with less range in size (0.04 to 0.12 ha). The lower spread of error in the Drake et al. model is most likely explained by their use of relatively large old-growth forest plots (n = 18, 0.5 ha), while our old-growth plots were much smaller and numerous (n = 43, 0.09 ha). In old-growth forests, large plots should smooth the spatial variability in both field-measured biomass and lidar heights at short distances, thereby reducing residual error in the model at higher biomass levels.

When considering the full range of biomass (all plots), the best model with two lidar metrics included MeanHgt and MaxHgt and was slightly better than the model using only MeanHgt ($r^2 = 0.90$ two variables vs. $r^2 = 0.88$ one variable). We used the MeanHgt–MaxHgt model to map biomass, which revealed detailed variation across the landscape (Fig. 6). The northern part of La Selva has a mix of plantations and abandoned pastures, with relatively low biomass values (Fig. 6A). The western side of the map covers a secondary forest with moderate values (Fig. 6B). The old-growth forest covers most of the lidar dataset (Fig. 6C). Biomass values are relatively high, but there are areas with low biomass in large canopy gaps in areas with swamps and large tree falls. Some north–south streaks are evident where there were no lidar returns, so the DCM had artificially low heights (see Clark et al., 2004).

These results using lidar metrics are encouraging as the metrics are relatively simple to compute from lidar-derived vegetation height, whether from raster DCMs or the lidar *xyz* point cloud. A challenge to using lidar sensors over tropical rain forests is retrieving ground returns from the original lidar *xyz* point cloud or derived raster surface, which is a prerequisite to calculating accurate vegetation heights (Clark et al., 2004). Dense canopy and understory vegetation in tropical rain forests makes retrieving lidar returns from bare ground difficult, especially with the first discrete-return type sensor used in this study (Clark et al., 2004). There are now commercial lidar

Table 6
Plantation plots only: top regression models to estimate aboveground biomass from lidar and hyperspectral metrics. All models are with OLS regression, Sqrt transformation of biomass.

Sensors	X1	X2	r^2	RMSE[a]	Intercept	Slope X1	Slope X2
Plantation plots located on FLIMAP image (n = 32)							
Lidar	MeanHgt	–	0.95	11.1	0.48	0.55	–
Lidar	MeanHgt	Skewness	0.96	10.8	0.31	0.60	0.16
Plantation plots located on both FLIMAP and HYDICE images (n = 15)							
One predictor variable							
Lidar	MeanHgt	–	0.96	11.5	0.48	0.55	–
Hyper	EVI	–	0.64	22.7	−1.88	83.21	–
Two predictor variables							
Lidar	Mean95pct	StdDevHgt	0.98	8.1	0.42	0.73	−1.75
Hyper	GV	NDWI	0.78	20.2	−5.09	0.03	−42.55
Lidar + Hyper	MeanHgt	RVSI	0.98	8.7	−0.09	0.47	79.56

[a] RMSE = root mean-squared error in biomass units, Mg/Ha.

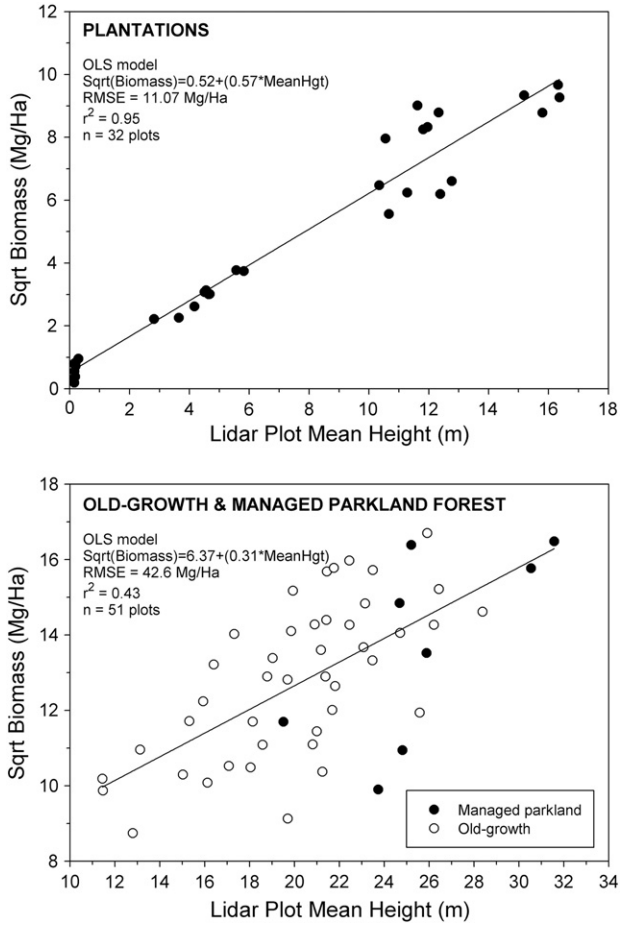

Fig. 5. Ordinary least-squares regression model for estimating plot-level biomass (square-root) from lidar-derived plot mean height (MeanHgt), for plots in plantations and managed parkland/old-growth forest.

sensors that record multiple discrete returns, which typically include a last return and have relatively high point density. These sensors will undoubtedly make ground-retrieval in tropical rain forests more accurate. Improvements in ground-retrieval should strengthen biomass estimation models by reducing RMSE. Further experiments should analyze the optimal lidar footprint size and density to adequately retrieve the ground, derive canopy heights, and the subsequent sensitivity of biomass estimates to these parameters.

We found that hyperspectral metrics provided lower accuracy in estimating biomass than lidar metrics, whether with all plots or with the more accurate plantation plots. Models with two hyperspectral metrics performed slightly better than models with one hyperspectral metric, although even these models had poorer performance than models with single lidar metrics. Furthermore, the best model with a single lidar and hyperspectral metric was no better than the best model using two lidar metrics, with either all plots or plantations only. For our remote sensing datasets, suite of metrics and tropical rain forest site, hyperspectral data did not improve biomass estimation models, and so these data were not worth the additional cost and time needed for acquisition and processing.

Although they did not improve biomass estimation, the hyperspectral metrics selected in the regression models were a mix of indices that track green vegetation and structure (i.e., SR, NDVI, EVI, and GV), canopy water (WBI and NDWI), leaf and fruit senescence (PSRI) and lignin concentrations (NDLI). The NDLI was the best hyperspectral metric for single-variable models using all plots, with NDLI values increasing sharply with biomass (Fig. 4). However, the linear relationship was heavily influenced by the 4 lowest biomass plots. These plots were from plantations with a 1-yr harvest cycle. The two lowest biomass plots also had the lowest NDLI values near 0.02 (Fig. 4), while the other two plots had slightly higher NDLI of 0.032 and 0.036. Harvest was conducted after biomass was measured in the field, making the relationship between lidar and hyperspectral metrics at this low end of biomass suspect. When the 2 lowest biomass plots were removed from the regression model, the model r^2 dropped from 0.49 to 0.26. Since the NDLI model is not robust without these low biomass plots, we do not discuss it further.

4.2. Leaf phenology and metric variability

An important consideration in these analyses is tree phenology, especially leaf senescence. Several species of canopy trees in old-growth forest were shedding leaves or leafless at the time of the hyperspectral flight in March, while more tree species had leaves when the FLI-MAP data were acquired in September (Frankie et al., 1974). Trunks and branches of large canopy trees are the dominant components of forest biomass, and tree-level biomass is typically estimated from general equations based on stem diameter without considering leaf phenology. However, leaf phenology causes temporal variation in hyperspectral and lidar metrics even though plot biomass remains relatively stable throughout the year; and thus, relationships between metrics and biomass will change depending on the time of year that the sensors are flown.

If our lidar sensor had been flown when there was a greater percentage of leafless trees in the canopy (i.e., January through March), and we assume that ground retrieval accuracy remains constant, we would expect more canopy lidar returns from deeper in the canopy and lower values for MeanHgt, MedianHgt and MedMax and increasing values of StdDevHgt. Plot-scale metrics such as MaxHgt and Mean95pct height should be less affected by leaf phenology because large branches continue to cause upper-canopy returns when trees are leafless, especially with a lidar sensor offering high point density (Brandtberg et al., 2003; Clark, 2007). Future research should investigate how the lidar–biomass relationship varies with levels of canopy deciduousness and point density (Drake et al., 2003).

Tree leaf phenology is also an important consideration with hyperspectral metrics. First, a decrease in canopy leaves, or LAI, changes the fractional spectral mixture of an individual species' leaves, bark, fruits and flowers, understory vegetation and soil, and canopy lianas (vines), moss and lichen, within the sensor instantaneous field of view (IFOV). For example, chlorophyll and NIR water absorption features from green leaves are expressed more deeply in the photon scattering environment provided by high LAI canopies (Asner, 1998). In contrast, SWIR absorptions from protein, nitrogen, starch, lignin, cellulose, and sugars (Curran, 1989; Elvidge, 1990) are typically obscured by heavy water absorption in high LAI canopies. Thus, as an old-growth tropical forest enters a season with a relatively high fractional cover of senescing leaves or exposed branches in the canopy, we would expect chlorophyll and water absorption metrics (e.g., EVI and WBI) to decrease and SWIR absorption metrics (e.g., NDLI) to increase, while biomass remains relatively stable.

In fusing hyperspectral and lidar data for biomass estimation, one of the best uses of the hyperspectral information may be to adjust the lidar predictive models for species or canopy state (Anderson et al., 2008; Swatantran et al., *in press*). For species-rich continental tropical rain forests, it is currently unrealistic to classify all canopy tree species from hyperspectral data (Clark et al., 2005), nor do we have a wide range of allometric biomass equations for tropical species. However, there is potential to map the fractional cover of canopy senescence or deciduousness, perhaps through a metric such as NPV (Bohlman, 2008). This type of analysis was not possible with our lidar and hyperspectral datasets as they were flown at two different seasons, with large differences in canopy phenology. However, this analysis

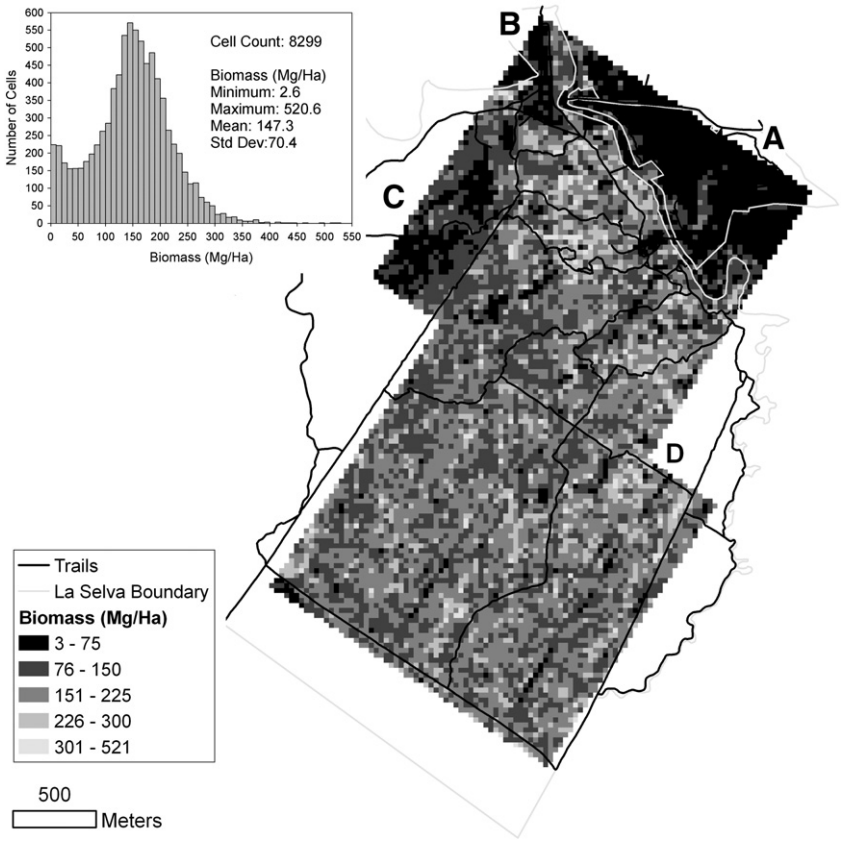

Fig. 6. Estimated aboveground biomass (Mg/Ha) across the La Selva landscape, which includes A. abandoned pastures, B. plantations, C. secondary forests, and D. old-growth forests. Inset is the histogram from all 8299 30×30 m cells in the biomass map.

would be possible with simultaneous (or nearly so) acquisition of lidar and hyperspectral data, such as that provided by the Carnegie Airborne Observatory (Asner et al., 2007; Asner et al., 2008b).

5. Conclusion

The goal of this study was to assess small-footprint lidar and hyperspectral metrics for estimating aboveground biomass over a tropical rain forest landscape. Relatively simple lidar metrics derived from canopy heights within plots, such as mean height, had an impressive capacity to estimate biomass over a range of values. This study supports conclusions from studies at this and other climate zones that lidar is a premier instrument for mapping biomass (i.e., carbon stocks) across broad spatial scales (Anderson et al., 2008; Drake et al., 2002, 2003; Swatantran et al., in press). In agreement with conclusions by Swatantran et al. (in press) for a temperature forest site, hyperspectral metrics provided no additional benefit for estimating biomass in our tropical rain forest landscape.

Ultimately, a spaceborne system will be needed to map carbon stocks and flux at the broad spatial scales needed to support global carbon-emission regulation (Houghton, 2005; Rosenqvist et al., 2003). We suggest that future work in tropical forests should explore the sensitivity of lidar metrics to canopy-level leaf phenology, which varies throughout the year, and improving ground-retrieval accuracy. Newer lidar sensors that can sample at high point densities and record last discrete returns will help resolve these research questions. Hyperspectral sensors may be best suited for adjusting lidar-based biomass estimation equations for vegetation phenology or stress, as long as the sensors are flown simultaneously or close in time. Well-calibrated hyperspectral sensors, covering the full range of wavelengths from visible to shortwave-infrared energy, can take advantage of biochemical absorption properties that are expressed with varying levels of canopy LAI due to stress or seasonality. Taken together, airborne lidar and hyperspectral sensors will play an important role in determining sensor parameters for future spaceborne sensors.

Acknowledgments

This research was funded in part by "Multisite Integration of LIDAR and Hyperspectral Data for Improved Estimation of Carbon Stocks and Exchanges", (P.I. Dar Roberts), NASA Carbon Cycle Science grant (NNG05GE56G). The collection of old-growth tree data from CARBONO plots was funded by the National Science Foundation under Grant DEB-0129038 and the Andrew W. Mellon Foundation. Funding to measure plantation biomass data came from National Science Foundation award DEB-9975235 and the Andrew W. Mellon Foundation. Arboretum stem data were collected by Orlando Vargas, OTS. HYDICE and lidar data were donated to OTS by the U.S. Spectral Information Technology Application Center (SITAC) and U.S. Army Corps of Engineers Topographic Engineering Center, respectively.

References

Anderson, J. E., Plourde, L. C., Martin, M. E., Braswell, B. H., Smith, M. L., Dubayah, R. O., Hofton, M. A., & Blair, J. B. (2008). Integrating waveform lidar with hyperspectral imagery for inventory of a northern temperate forest. *Remote Sensing of Environment*, *112*(4), 1856–1870.

Angelsen, A., Brown, S., Loisel, C., Peskett, L., Streck, C., & Zarin, D. (2009). *Reducing Emissions from Deforestation and Forest Degradation (REDD): an options assessment report.* Washington, DC: Meridian Institute.

Asner, G. P. (1998). Biophysical and biochemical sources of variability in canopy reflectance. *Remote Sensing of Environment*, *64*(3), 234–253.

Asner, G. P., Jones, M. O., Martin, R. E., Knapp, D. E., & Hughes, F. R. (2008a). Remote sensing of native and invasive species in Hawaiian forests. *Remote Sensing of Environment*, *112*, 1912–1926.

Asner, G. P., Knapp, D. E., Jones, M. O., Kennedy-Bowdoin, T., Martin, R. E., Boardman, J., & Field, C. B. (2007). Carnegie Airborne Observatory: In-flight fusion of hyperspectral

imaging and waveform light detection and ranging (wLiDAR) for three-dimensional studies of ecosystems. *Journal of Applied Remote Sensing*, *1*. doi:10.1117/1.2794018.
Asner, G. P., Knapp, D. E., Kennedy-Bowdoin, T., Jones, M. O., Martin, R. E., Boardman, J., & Hughes, R. F. (2008b). Invasive species detection in Hawaiian rainforests using airborne imaging spectroscopy and LiDAR. *Remote Sensing of Environment*, *112*, 1942–1955.
Asner, G. P., & Lobell, D. B. (2000). A biogeophysical approach for automated SWIR unmixing of soils and vegetation. *Remote Sensing of Environment*, *74*(1), 99–112.
Asner, G. P., Martin, R. E., Carlson, K. M., Rascher, U., & Vitousek, P. M. (2006). Vegetation–climate interactions among native and invasive species in Hawaiian rainforest. *Ecosystems*, *9*, 1106–1117.
Asner, G. P., & Vitousek, P. M. (2005). Remote analysis of biological invasion and biogeochemical change. *Proc. Natl. Acad. Sci. USA*, *102*(12), 4383–4386.
Basedow, R. W., Carmer, D. C., & Anderson, M. E. (1995). *HYDICE system: Implementation and performance*, *Vol. 2480*, Orlando, FL, USA: SPIE Proceedings Feb. 17–24.
Blair, J. B., & Hofton, M. A. (1999). Modeling laser altimeter return waveforms over complex vegetation using high-resolution elevation data. *Geophysical Research Letters*, *26*, 2509–2512.
Bohlman, S. (2008). Hyperspectral remote sensing of exposed wood and deciduous trees in seasonal tropical forests. In M. Kalacska, & G. A. Sanchez-Azofeifa (Eds.), *Chapter 8 in hyperspectral remote sensing of tropical and sub-tropical forests* (pp. 177–192). New York: CRC Press.
Brandtberg, T., Warner, T. A., Landenberger, R. E., & McGraw, J. B. (2003). Detection and analysis of individual leaf-off tree crowns in small footprint, high sampling density lidar data from the eastern deciduous forest in North America. *Remote Sensing of Environment*, *85*(3), 290–303.
Brown, S. (1997). *Estimating biomass and biomass change of tropical forests: A primer. UN-FAO Forestry Paper 134*. Rome, Italy: UN-FAO.
Carlson, K. M., Asner, G. P., Hughes, R. F., Ostertag, R., & Martin, R. E. (2007). Hyperspectral remote sensing of canopy biodiversity in Hawaiian lowland rainforests. *Ecosystems*, *10*, 536–549.
Clark, M.L. (2005). An assessment of hyperspectral and lidar remote sensing for the monitoring of tropical rain forest trees. Doctoral Dissertation, University of California, Santa Barbara, USA, 319 pp.
Clark, M. L. (2007). Relative advantages of airborne lidar and hyperspectral data for individual tropical tree classification. *Proceedings of the 32nd International Symposium on Remote Sensing of Environment, June 25–29* San Jose, Costa Rica.
Clark, D. B., & Clark, D. A. (2000). Landscape-scale variation in forest structure and biomass in a tropical rain forest. *Forest Ecology and Management*, *137*(1–3), 185–198.
Clark, D. B., Clark, D. A., Rich, P. M., Weiss, S., & Oberbauer, S. F. (1996). Landscape scale evaluation of understory light and canopy structure: Methods and application in a neotropical lowland rain forest. *Canadian Journal of Forest Research*, *26*(5), 747–757.
Clark, M. L., Clark, D. B., & Roberts, D. A. (2004). Small-footprint lidar estimation of sub-canopy elevation and tree height in a tropical rain forest landscape. *Remote Sensing of Environment*, *91*(1), 68–89.
Clark, M. L., Roberts, D. A., & Clark, D. B. (2005). Hyperspectral discrimination of tropical rain forest tree species at leaf to crown scales. *Remote Sensing of Environment*, *96*(3–4), 375–398.
Cole, T. G., & Ewel, J. J. (2006). Allometric equations for four valuable tropical tree species. *Forest Ecology and Management*, *229*, 351–360.
Cressie, N. A. C. (1993). *Statistics for spatial data.* Inc, New York: John Wiley & Sons.
Curran, P. J. (1989). Remote sensing of foliar chemistry. *Remote Sensing of Environment*, *30*(3), 271–278.
DeFries, R., Achard, F., Brown, S., Herold, M., Murdiyarso, D., Schlamadinger, B., & de Souza Jr, C. (2007). Earth observations for estimating greenhouse gas emissions from deforestation in developing countries. *Environmental Science and Policy*, *10*, 385–394.
Dennison, P. E., Roberts, D. A., Thorgusen, S. R., Regelbrugge, J. C., Weise, D., & Lee, C. (2003). Modeling seasonal changes in live fuel moisture and equivalent water thickness using a cumulative water balance index. *Remote Sensing of Environment*, *88*(4), 442–452.
Dixon, R. K., Brown, S., Houghton, R. A., Solomon, A. M., Trexler, M. C., & Wisniewski, J. (1994). Carbon pools and flux of global forest eco-systems. *Science*, *263*(5144), 185–190.
Drake, J. B., Dubayah, R. O., Clark, D. B., Knox, R. G., Blair, J. B., Hofton, M. A., Chazdon, R. L., Weishampel, J. F., & Prince, S. D. (2002). Estimation of tropical forest structural characteristics using large-footprint lidar. *Remote Sensing of Environment*, *79*, 305–319.
Drake, J. B., Knox, R. G., Dubayah, R. O., Clark, D. B., Condit, R., Blair, J. B., & Hofton, M. A. (2003). Above-ground biomass estimation in closed canopy neotropical forests using lidar remote sensing: Factors affecting the generality of relationships. *Global Ecology and Biogeography*, *12*, 147–159.
Elvidge, C. D. (1990). Visible and near-infrared reflectance characteristics of dry plant materials. *International Journal of Remote Sensing*, *11*(10), 1775–1795.
Elvidge, C. D., & Chen, Z. K. (1995). Comparison of broadband and narrowband red and near-infrared vegetation indexes. *Remote Sensing of Environment*, *54*(1), 38–48.
Foody, G. M., Boyd, D. S., & Cutler, M. E. J. (2003). Predictive relations of tropical forest biomass from Landsat TM data and their transferability between regions. *Remote Sensing of Environment*, *85*(4), 463–474.
Frankie, G. W., Baker, H. G., & Opler, P. A. (1974). Comparative phenological studies of trees in tropical wet and dry forests in the lowlands of Costa Rica. *Journal of Ecology*, *62*(3), 881–919.
Gao, B. C. (1996). NDWI — A normalized difference water index for remote sensing of vegetation liquid water from space. *Remote Sensing of Environment*, *58*(3), 257–266.
Hall, F. G., Huemmrich, K. F., Goetz, S. J., Sellers, P. J., & Nickeson, J. E. (1992). Satellite remote sensing of surface energy balance: Success, failures, and unresolved issues in FIFE. *Journal of Geophysical Research*, *97*(D17), 19,061–19,089.
Hall, F. G., Shimabukuro, Y. E., & Huemmrich, K. F. (1995). Remote sensing of forest biophysical structure using mixture decomposition and geometric reflectance models. *Ecological Applications*, *5*(4), 993–1013.
Holdridge, L. R. (1971). *Forest environments in tropical life zones: A pilot study*. New York: Pergamon Press.
Houghton, R. A. (2005). Aboveground forest biomass and the global carbon balance. *Global Change Biology*, *11*, 945–958.
Huete, A. R. (1988). A Soil Adjusted Vegetation Index (SAVI). *Remote Sensing of Environment*, *25*(3), 295–309.
Huete, A., Didan, K., Miura, T., Rodriguez, E. P., Gao, X., & Ferreira, L. G. (2002). Overview of the radiometric and biophysical performance of the MODIS vegetation indices. *Remote Sensing of Environment*, *83*(1–2), 195–213.
Huete, A. R., Jackson, R. D., & Post, D. F. (1985). Spectral response of a plant canopy with different soil backgrounds. *Remote Sensing of Environment*, *17*, 37–53.
Imhoff, M. L. (1995). Radar backscatter and biomass saturation — Ramifications for global biomass inventory. *IEEE Transactions on Geoscience and Remote Sensing*, *33*(2), 511–518.
Jordan, C. F. (1969). Derivation of Leaf-Area Index from quality of light on the forest floor. *Ecology*, *50*(4), 663–666.
Kalacska, M., Bohlman, S., Sanchez-Azofeifa, G. A., Castro-Esau, K., & Caelli, T. (2007a). Hyperspectral discrimination of tropical dry forest lianas and trees: Comparative data reduction approaches at the leaf and canopy levels. *Remote Sensing of Environment*, *109*, 406–415.
Kalacska, M., Sanchez-Azofeifa, G. A., Rivard, B., Caelli, T., White, H. P., & Calvo-Alvarado, J. C. (2007b). Ecological fingerprinting of ecosystem succession: Estimating secondary tropical dry forest structure and diversity using imaging spectroscopy. *Remote Sensing of Environment*, *108*, 82–96.
Kasischke, E. S., Melack, J. M., & Dobson, M. C. (1997). The use of imaging radars for ecological applications — A review. *Remote Sensing of Environment*, *59*(2), 141–156.
Keshava, N., & Mustard, J. F. (2002). Spectral unmixing. *IEEE Signal Processing Magazine*, *19*(1), 44–57.
Koetz, B., Sun, G., Morsdorf, F., Ranson, K. J., Kneubühler, M., Itten, K., & Allgöwer, B. (2007). Fusion of imaging spectrometer and LIDAR data over combined radiative transfer models for forest canopy characterization. *Remote Sensing of Environment*, *106*, 449–459.
Lark, R. M. (2000). Regression analysis with spatially autocorrelated error: Simulation studies and application to mapping of soil organic matter. *International Journal of Geographical Information Science*, *14*(3), 247–264.
Lark, R. M., & Cullis, B. R. (2004). Model-based analysis using REML for inference from systematically sampled data on soil. *European Journal of Soil Science*, *55*(4), 799–813.
Lefsky, M. A., Cohen, W. B., Harding, D. J., Parker, G. G., Acker, S. A., & Gower, S. T. (2002a). Lidar remote sensing of above-ground biomass in three biomes. *Global Ecology and Biogeography*, *11*(5), 393–399.
Lefsky, M. A., Cohen, W. B., Parker, G. G., & Harding, D. J. (2002b). Lidar remote sensing for ecosystem studies. *Bioscience*, *52*(1), 19–30.
Lefsky, M. A., Keller, M., Panga, Y., de Camargo, P. B., & Hunter, M. O. (2007). Revised method for forest canopy height estimation from Geoscience Laser Altimeter System waveforms. *Journal of Applied Remote Sensing*, *1*, 1–18.
Lucas, R., Bunting, P., Paterson, M., & Chisholm, L. (2008). Classification of Australian forest communities using aerial photography, CASI and HyMap data. *Remote Sensing of Environment*, *112*, 2088–2103.
Luckman, A., Baker, J., Kuplich, T. M., Yanasse, C. D. F., & Frery, A. C. (1997). A study of the relationship between radar backscatter and regenerating tropical forest biomass for spaceborne SAR instruments. *Remote Sensing of Environment*, *60*(1), 1–13.
McGwire, K., Minor, T., & Fenstermaker, L. (2000). Hyperspectral mixture modeling for quantifying sparse vegetation cover in arid environments. *Remote Sensing of Environment*, *72*(3), 360–374.
Menalled, F. D., Kelty, M. J., & Ewel, J. J. (1998). Canopy development in tropical tree plantations: A comparison of species mixtures and monocultures. *Forest Ecology and Management*, *104*, 249–263.
Merton, R., & Huntington., J. (1999). *Early simulation results of the ARIES-1 satellite sensor for multi-temporal vegetation research derived from AVIRIS*. Pasadena, CA: NASA Jet Propulsion Lab Available at ftp://popo.jpl.nasa.gov/pub/docs/workshops/99_docs/41.pdf (verified 8 Apr. 2008).
Merzlyak, M. N., Gitelson, A., Chivkunova, O. B., & Rakitin, V. Y. (1999). Non-destructive optical detection of pigment changes during leaf senescence and fruit ripening. *Physiologica Plantarum*, *106*, 135–141.
Myneni, R. B., Hall, F. G., Sellers, P. J., & Marshak, A. L. (1995). The interpretation of spectral vegetation indexes. *IEEE Transactions on Geoscience and Remote Sensing*, *33*, 481–486.
Næsset, E. (1997). Determination of mean tree height of forest stands using airborne laser scanner data. *ISPRS Journal of Photogrammetry and Remote Sensing*, *52*, 49–56.
Nepstad, D., Veríssimo, A., Alencar, A., Nobre, C., Lima, E., Lefebvre, P., Schlesinger, P., Potterk, C., Moutinho, P., Mendoza, E., Cochrane, M., & Brooks, V. (1999). Large-scale impoverishment of Amazonian forests by logging and fire. *Nature*, *398*, 505–508.
Nilsson, M. (1996). Estimation of tree heights and stand volume using an airborne lidar system. *Remote Sensing of Environment*, *56*(1), 1–7.
Peddle, D. R., Brunke, S. P., & Hall, F. G. (2001). A comparison of spectral mixture analysis and ten vegetation indices for estimating boreal forest biophysical information from airborne data. *Canadian Journal of Remote Sensing*, *27*(6), 627–635.
Peñuelas, J., Pinol, J., Ogaya, R., & Filella, I. (1997). Estimation of plant water concentration by the reflectance water index WI (R900/R970). *International Journal of Remote Sensing*, *18*(13), 2869–2875.
Perry, E. M., & Roberts, D. A. (2008). Sensitivity of narrow-band and broad-band indices for assessing nitrogen availability and water stress in annual crop. *Agronomy Journal.*, *100*(4), 1211–1219.

Pinheiro, J. C., & Bates, D. M. (2000). *Mixed-effects models in S and S-plus.* New York: Springer-Verlag.

R Development Core Team (2005). *R: A language and environment for statistical computing.* Vienna, Austria: R Foundation for Statistical Computing ISBN 3-900051-07-0, http://www.R-project.org

Ribeiro, P. J., Jr., & Diggle, P. J. (2001). *geoR: A package for geostatistical analysis. R-NEWS*, *Vol 1*, No 2, ISSN 1609-3631.

Roberts, D. A., Smith, M. O., & Adams, J. B. (1993). Green vegetation, nonphotosynthetic vegetation, and soils in AVIRIS data. *Remote Sensing of Environment*, *44*(2–3), 255–269.

Roberts, D. A., Ustin, S. L., Ogunjemiyo, S., Greenberg, J., Dobrowski, S. Z., Chen, J., & Hinckley, T. M. (2004). Spectral and structural measures of northwest forest vegetation at leaf to landscape scales. *Ecosystems*, *7*(5), 545–562.

Rosenqvist, A., Milne, A., Lucas, R., Imhoff, M., & Dobson, C. (2003). A review of remote sensing technology in support of the Kyoto Protocol. *Environmental Science and Policy*, *6*, 441–455.

Rouse, J. W., Haas, R. H., Schell, J. A., & Deering, D. W. (1973). Monitoring vegetation systems in the great plains with ERTS. *Third ERTS Symposium, NASA SP-351*, *volume 1*. (pp. 309–317).

Saatchi, S. S., Houghton, R. A., Dos Santos Alvala, R. C., Soares, J. V., & Yu, Y. (2007). Distribution of aboveground live biomass in the Amazon basin. *Global Change Biology*, *13*, 816–837.

Sader, S. A., Waide, R. B., Lawrence, W. T., & Joyce, A. T. (1989). Tropical forest biomass and successional age class relationships to a vegetation index derived from Landsat TM data. *Remote Sensing of Environment*, *28*, 143–156.

Santos, J. R., Freitas, C. C., Araujo, L. S., Dutra, L. V., Mura, J. C., Gama, F. F., Soler, L. S., & Sant'Anna, S. J. S. (2003). Airborne P-band SAR applied to the aboveground biomass studies in the Brazilian tropical rainforest. *Remote Sensing of Environment*, *87*(4), 482–493.

Serrano, L., Peñuelas, J., & Ustin, S. (2002). Remote sensing of nitrogen and lignin in Mediterranean vegetation from AVIRIS data: Decomposing biochemical from structural signals. *Remote Sensing of Environment*, *81*, 355–364.

Serrano, L., Ustin, S. L., Roberts, D. A., Gamon, J. A., & Peñuelas, J. (2000). Deriving water content of chaparral vegetation from AVIRIS data. *Remote Sensing of Environment*, *74*(3), 570–581.

Sonnentag, O., Chen, J. M., Roberts, D. A., Talbot, J., Halligan, K. Q., & Govind, A. (2007). Mapping tree and shrub leaf area indices in an ombrotrophic peatland through multiple endmember spectral unmixing. *Remote Sensing of Environment*, *109*(3), 342–360.

Spanner, M., Johnson, L., Miller, J., McCreight, R., Freemantle, J., Runyon, J., & Gong, P. (1994). Remote-sensing of seasonal Leaf-Area Index across the Oregon transect. *Ecological Applications*, *4*(2), 258–271.

Steininger, M. K. (2000). Satellite estimation of tropical secondary forest aboveground biomass: Data from Brazil and Bolivia. *International Journal of Remote Sensing*, *21*(6), 1139–1157.

Swatantran, A., Dubayah, R., Roberts, D., Hofton, M., & Blair, J. B. (2011-this issue). Mapping biomass and stress in the Sierra Nevada using lidar and hyperspectral data fusion. *Remote Sensing of Environment*, *115*, 2917–2930.

Tucker, C. J. (1979). Red and photographic infrared linear combinations for monitoring vegetation. *Remote Sensing of Environment*, *8*(2), 127–150.

Vargas, O. (2005). *Botanist, La Selva Biological Station, Organization for Tropical Studies.* Costa Rica: Personal communication.

Wang, Q., Adiku, S., Tenhunen, J., & Granier, A. (2005). On the relationship of NDVI with leaf area index in a deciduous forest site. *Remote Sensing of Environment*, *94*, 244–255.